

This document is confidential and is proprietary to the American Chemical Society and its authors. Do not copy or disclose without written permission. If you have received this item in error, notify the sender and delete all copies.

YS-TaS₂ and YxLa_{1-x}S-TaS₂ (0 ≤ x ≤ 1) Nanotubes: A Family of Misfit Layered Compounds

Journal:	<i>ACS Nano</i>
Manuscript ID	nn-2019-09284q.R3
Manuscript Type:	Article
Date Submitted by the Author:	n/a
Complete List of Authors:	Hettler, Simon; Universidad de Zaragoza Sreedhara, M. B.; Weizmann Institute of Science, Materials and Interfaces Serra, Marco; Weizmann Institute of Science Sinha, Sudarson; Weizmann Institute of Science Popovitz-Biro, Ronit; Weizmann Institute of Science, Electron Microscopy Unit, Pinkas, Iddo; Weizmann Institute of Science, Dept. Plant Sciences Enyashin, Andrey; Institut himii tverdogo tela UrO RAN, Laboratory of Quantum Chemistry and Spectroscopy Tenne, Reshef; Weizmann Institute of Science, Materials and Interfaces Arenal, Raul; Universidad de Zaragoza, Instituto de Nanociencia de Aragon

SCHOLARONE™
Manuscripts

YS-TaS₂ and Y_xLa_{1-x}S-TaS₂ (0 ≤ x ≤ 1) Nanotubes: A Family of Misfit Layered Compounds

Simon Hettler^{1*}, M. B. Sreedhara^{2*}, Marco Serra^{2,3}, Sudarson S. Sinha², Ronit Popovitz-Biro², Iddo Pinkas^{2a}, Andrey N. Enyashin^{4,5#}, Reshef Tenne^{2#} and Raul Arenal^{1,6,7#}

¹ Instituto de Nanociencia de Aragón, Universidad de Zaragoza, 50018 Zaragoza, Spain

² Department of Materials and Interfaces, ^{2a}Department of Chemical Research Support, Weizmann Institute of Science, Rehovot 76100, Israel

³ Department of Physical Chemistry, Center for Biomedical Research (CINBIO), Universidad de Vigo, 36310, Spain

⁴ Institute of Solid State Chemistry UB RAS, 620990 Ekaterinburg, Russian Federation

⁵ Ural Federal University, Institute of Natural Sciences and Mathematics, 620083 Ekaterinburg, Russian Federation

⁶ Instituto de Ciencias de Materiales Aragón, CSIC-U. Zaragoza, 50009 Zaragoza, Spain

⁷ ARAID Foundation, 50018 Zaragoza, Spain

*Equal contribution

#Corresponding authors

Reshef Tenne (ORCID [0000-0003-4071-0325](https://orcid.org/0000-0003-4071-0325)) reshef.tenne@weizmann.ac.il

Raul Arenal (ORCID [0000-0002-2071-9093](https://orcid.org/0000-0002-2071-9093)) arenal@unizar.es

Andrey N. Enyashin (ORCID [0000-0001-6195-7971](https://orcid.org/0000-0001-6195-7971)) enyashin@ihim.uran.ru

S. Hettler (ORCID [0000-0002-9102-7895](https://orcid.org/0000-0002-9102-7895))

M. B. Sreedhara (ORCID [0000-0003-4925-4346](https://orcid.org/0000-0003-4925-4346))

M. Serra (ORCID [0000-0002-6816-4947](https://orcid.org/0000-0002-6816-4947))

S. S. Sinha (ORCID [0000-0002-0831-2338](https://orcid.org/0000-0002-0831-2338))

I. Pinkas (ORCID [0000-0001-7434-9844](https://orcid.org/0000-0001-7434-9844))

This work is dedicated to Prof. C.N.R. Rao- a scholar and mentor on the occasion of his 85th birthday

Abstract

We present the analysis of a family of nanotubes (NTs) based on the quaternary misfit layered compound (MLC) Y_xLa_{1-x}S-TaS₂. The NTs were successfully synthesized within the whole range of possible compositions *via* the chemical vapor transport technique. In-depth analysis of the NTs using electron microscopy and spectroscopy proves the in-phase (partial) substitution of La by Y in the (La,Y)S subsystem and reveals structural changes compared to the previously reported LaS-TaS₂ MLC-NTs. The observed structure can be linked to the slightly different lattice parameters of LaS and YS. Raman spectroscopy and infrared transmission measurements reveal the tunability of the plasmonic and vibrational properties. Density-functional theory calculations showed that the Y_xLa_{1-x}S-TaS₂ MLCs are stable in all compositions. Moreover, the calculations indicated that substitution of La by Sc atoms is electronically not favorable, which explains our failed attempt to synthesize these MLC and NTs thereof.

Keywords: inorganic nanotubes, misfit layered compounds, electron microscopy, electron spectroscopy, Raman spectroscopy, charge transfer, density-functional theory

The observation of fullerene-like structures and nanotubes (NTs) formed by the layered compound WS_2 ¹ has instigated a lot of research dedicated to inorganic nanomaterials.²⁻⁴ Among these, misfit layered compounds (MLC) play a special role. Microtubules based on MLC were reported early-on.⁵ More recently, several solid-state strategies for the syntheses of various MLC nanotubes were described.⁶⁻⁸ MLC consist of two different layered oxides or chalcogenides which are stacked alternately along their *c* direction. In case of chalcogenide MLCs the stacking is composed of a metal chalcogenide (MX) with a distorted rock-salt structure and a transition-metal dichalcogenide (TX_2) with hexagonal structure (see **Fig. 1** for schematic presentation).⁹⁻¹² As both compounds exhibit their own symmetry, the stacking typically is incommensurate at least in one direction (*a* and/or *b*) yielding the chemical formula $(\text{MX})_{1+y}(\text{TX}_2)_m$ [$M = \text{Sn, Pb, Sb, Bi, rare earth atoms (Ln)}$; $T = \text{Sn, Ti, V, Cr, Nb, Ta}$; $X = \text{S, Se, Te}$; $0.08 < y < 0.32$; $m = 1, 2, 3$],^{3,4} which is denoted for simplicity as MX- TX_2 . The deviation from stoichiometry is calculated from the *a* lattice parameters according to the formula $1+y=2a_{\text{TX}_2}/a_{\text{MX}}$. The mismatch between the MX and TX_2 layers along the *a* and/or *b*-axis induces a strain, which is one important driving force for the formation of NTs and nanoscrolls.¹³ Combining this “structural” driving force with the “chemical” one, *i.e.* eliminating the dangling bonds of the rim atoms by folding the layer and seaming,^{1,2} facilitates the formation of MLC-NTs.

MLC-NTs are promising for applications, *e.g.* in the field of thermoelectricity, due to the complementary properties of the two layered compounds. The physical behavior of MLC at low temperatures did not receive much attention,^{14,15} let alone in their quasi-1D nanotubular form, which were reported more than a decade ago.^{16,17} Recently, a modified synthetic process of MLC-NTs permitted introducing additional elements to form quaternary compounds starting from LaS-TaS_2 ,¹⁸ by partial replacement of La by Sr¹⁹ in the MX sublattice, or of the transition metal in the TX_2 sublattice ($T=\text{Ta,Nb}$).²⁰ Furthermore, partial replacement of the sulfur atoms by selenium atoms led to NTs of the type LaS-TaSe_2 with La/Ta and S/Se superlattices.¹⁸

Here, the synthesis and analysis of a family of MLC, *i.e.* $\text{Y}_x\text{La}_{1-x}\text{S-TaS}_2$ ($0 \leq x \leq 1$) is described in both the bulk form and as NTs. The MLC compound $(\text{YS})_{1.23}\text{NbS}_2$ was studied before in its bulk form,²⁰ but not the analogous compound with Ta as the transition metal. The aim of the present study is to control the properties of MLC-NTs, which is sought to achieve by (partially) exchanging elements in the LaS-TaS_2 structure. In case of La, Y is a suitable element due to the chemical similarities between La(S) and Y(S). The gradual exchange of La by Y provides a pathway for fine control of the MLC structure, the degree of charge transfer from the MX slab to the TX_2 layer as well as the vibrational properties of the MX subunit. In return, these chemical and structural variations serve as a gauge of the free carrier density in the semimetallic TaS_2 layer and hence a tool for controlling the plasmonic wavelength of the 1D MLC nanostructures in the infrared (IR) range. This property may have relevance to future plasmonic technology in the IR range. The NTs are synthesized by chemical vapor transport (CVT) and are analyzed by electron microscopy and spectroscopy as well as Raman and Fourier transform infrared (FTIR) measurements. Density-functional theory (DFT) calculations are presented and the stability criteria for

these compounds are discussed. Interestingly, while the Y-containing MLC are found to be stable, MLC based on Sc are unstable and indeed, Sc-containing MLC could not be obtained by the CVT method. Presumably, the charge capacity of the TaS₂ layer is not sufficient for the full charge transfer from the Sc_xLa_{1-x}S layer, inhibiting the formation of a stable MLC lattice in this case.

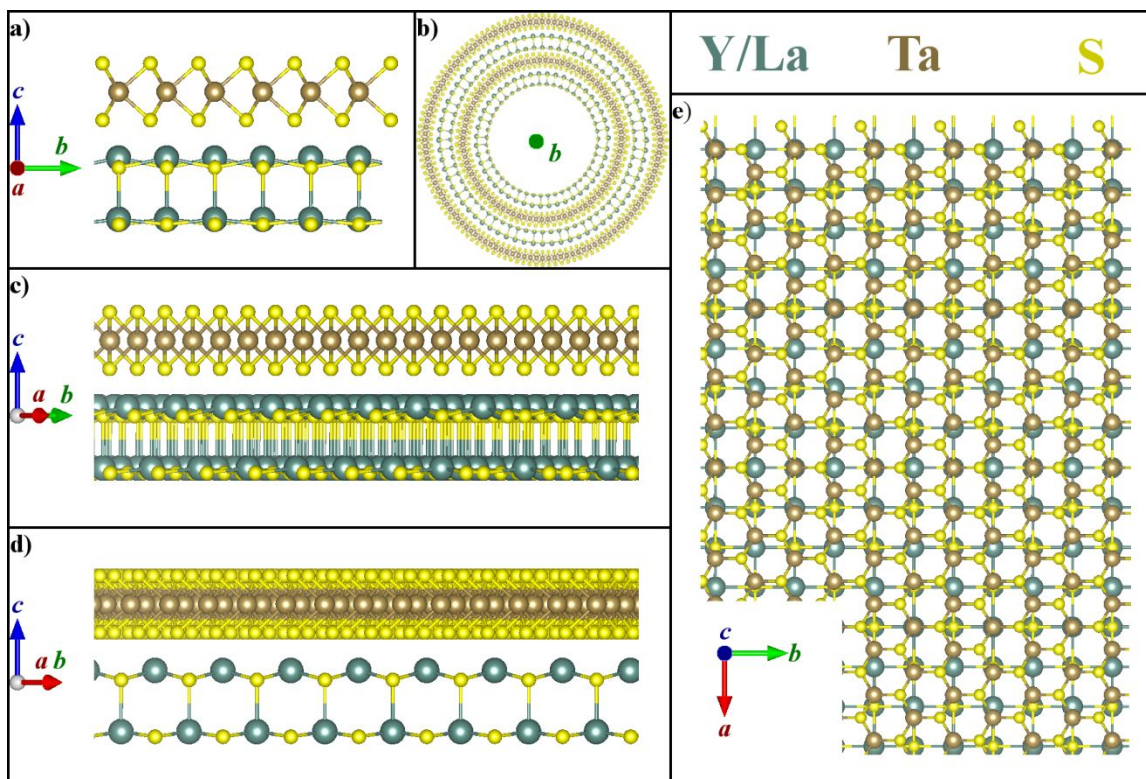


Figure 1. Schematic representation of the (Y,La)S-TaS₂ misfit structure stacked periodically along the *c*-axis depicted from different directions. (a) The view along *a* reveals that the lattices of (Y,La)S and TaS₂ have the same constant along *b*. (b) NT formed by two layers of the stack with the *b* axis coinciding with the tube axis. Rotation of the stack in (a) around *c* by (c) 30° and (d) 45° yields the [110] projection of TaS₂ and (Y,La)S, respectively. (e) The mismatch of MX (rock-salt) and TX₂ (hexagonal) along *a* direction is clearly visible by the view along the *c*-axis.

Results and Discussion

Microscopic structure and chemical analysis

Y_xLa_{1-x}S-TaS₂ NTs were successfully synthesized for yttrium-fractions of *x*=0.1 (10 at%), 0.2, 0.4, 0.6, 0.8, 0.9 and 1 and the corresponding samples are named Y10, Y20 ... Y100 in the following. **Fig. 2** shows two scanning electron microscopy (SEM) images of Y10 and Y100 samples revealing the presence of tubular structures and common by-products of the synthetic process, *i.e.* MLC platelets with the same composition. A selection of SEM images of all investigated samples can be found in **Fig. S1**, clearly revealing the successful synthesis of NTs for all values of *x*. The NTs appear hollow with varying length and

diameter. Quantitative analysis of the relative abundance (yield) of the NTs with respect to LaS-TaS₂ (x=0) was carried out *via* a detailed SEM analysis and is depicted in **Fig. 2c**. While NTs are observed for all analyzed samples with different Y content, the yield of the NTs varied between the different samples. The relative abundance generally drops with increasing Y content but shows a global maximum for x = 0.1 and a second local maximum for x = 0.8. The aspect ratio (length/width) of the NTs obtained by detailed transmission electron microscopy (TEM) analysis (analysis of over 20 NTs for each sample) is shown in the same graph (orange line in **Fig. 2c**). The aspect ratio of the NTs is the highest for x=0 and 1, *i.e.* the pure LaS-TaS₂ and YS-TaS₂ tubes and shows a minimum at x=0.2. For x>0.2, an almost linear relationship between the aspect ratio and x is observed, which allows to control this property of the NTs in the synthetic process.

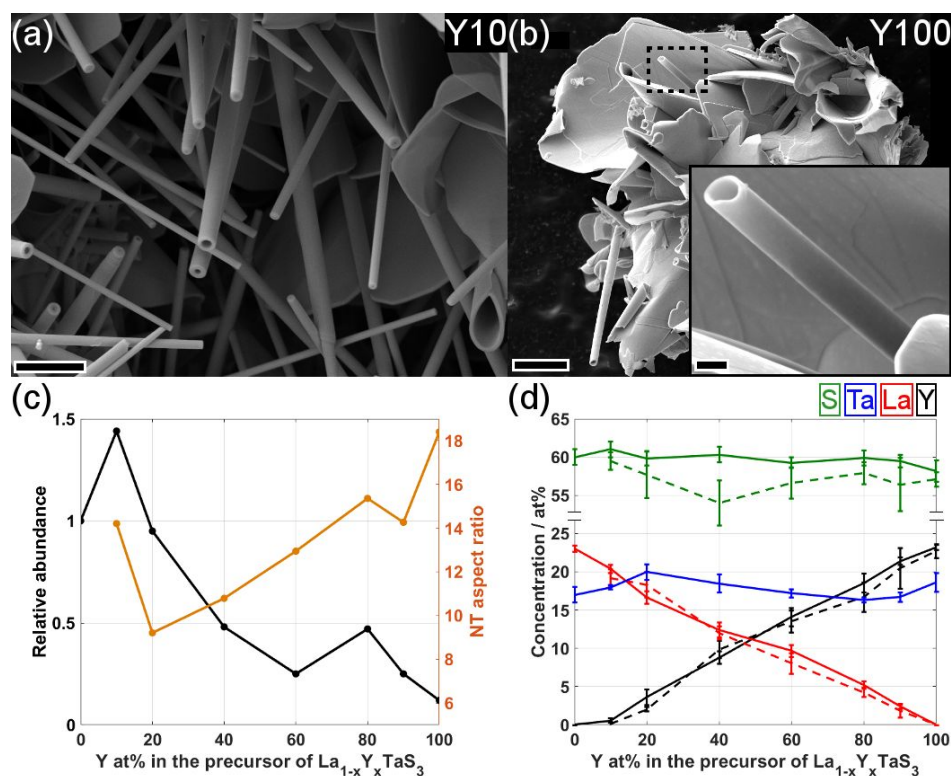


Figure 2. SEM micrographs of the tubular structures of (a) La_{0.9}Y_{0.1}S-TaS₂ (x=0.1) and (b) YS-TaS₂ (x=1) and the commonly observed by-products. Scrolling steps of the NTs' surface can be seen in (a). Scale bars are (a) 2 μ m, (b) 4 μ m and 400 nm (inset). (c) Relative abundance (by SEM analysis) and aspect ratio (by TEM analysis) of NTs as a function of Y at% in the MS part of the precursor. (d) Concentration of the elements in at% present in the Y_xLa_{1-x}TaS₃ misfit NTs as a function Y at% in the MS part of the precursor. The analysis was done by SEM-EDS (solid lines) as well as STEM-EDS (dashed lines). The error bar at each data point corresponds to the lower and higher limits of concentrations determined in a group of at least five NTs from the same batch.

1
2
3 The tube widths varied between 70 nm and 1200 nm and the lengths between 1 μm and
4 15 μm . The average sizes of the respective NTs can be inferred from **Table S1**. Besides
5 offering varying sizes, the NTs could be found in different shapes. The most common shape
6 ($>80\%$) is the standard tubular NT (**Fig. S2a**), which can have a single width throughout
7 its entire length. Alternatively, the NTs exhibit different widths, analogous to a telescope
8 (**Fig. S2b**). In addition to NTs, scrolls could be identified as well (**Fig. S2c and d**).
9
10

11 Semi-quantitative chemical analysis of the NTs was performed using energy-dispersive X-
12 ray spectroscopy (EDS)-SEM in order to determine the atomic composition of the NTs.
13 **Fig. S3-S5** show the EDS spectra of Y20, Y60 and Y100 samples. The main chemical
14 entities La, Y, Ta and S are observed, as well as small traces ($<1\%$) of Cl, which was
15 used as a transport agent. **Fig. 2d** summarizes the atomic concentration of each element as
16 a function of Y (at%) content in the precursor (with respect to the La content in the metal
17 sulfide (MS) unit). This analysis reveals that the Y content in the NTs exhibits an almost
18 linear relationship with the Y content in the precursor. It implies that Y substitutes easily
19 the La in the MS slab without appreciable lattice distortion. This situation is entirely
20 different from the case of Nb substitution into the Ta site of the TX_2 unit.²¹ In this case, the
21 Nb content of the MLC (and NTs) was very small up to 60 at% Nb in the precursor. Beyond
22 that level, the niobium substitution of the Ta in the TaS_2 of the NT lattice increased sharply.
23 Note however that in this case, the TX_2 unit of the Nb-rich NTs revealed a transformation
24 from the 2H (hexagonal coordination) to 1T (octahedral coordination) polytype, which is
25 quite uncommon in TaS_2 -based MLC.^{22,23}
26
27
28
29
30

31 In addition to SEM-EDS, chemical analysis was also performed by scanning (S)TEM-EDS
32 for several NTs from all the samples in order to determine their average composition. Three
33 exemplary spectra are depicted in **Fig. S6** and the results are summarized in **Table S1**. The
34 values obtained for Y, La and S have been added as dashed lines to **Fig. 2d**. Ta is omitted
35 in the plot as the analyzed Ta-L edge overlaps with the Cu-K signal stemming from the
36 TEM support grid. The concentrations determined by this technique and their dependence
37 on the composition (x) agree well with the results obtained by SEM-EDS (**Fig. 2d**).
38 Although the Y content increases linearly with x , the intended ratio between Y and La was
39 only correctly attained for $x > 0.2$. Especially the Y/La ratio in the NTs of Y10 was found
40 to be very low (2/98). Together with the high relative abundance of the Y10 sample, the
41 findings suggest that the stability of LaS-TaS₂ NTs can be increased by doping with a few
42 at% of Y. This doping seems to be favorable in comparison to the incorporation of a
43 considerable amount of Y ($> 1-2\%$) and the accompanying distortion of the LaS lattice
44 due to the smaller atomic radius of Y. Although small amounts of oxygen were detected in
45 STEM-EDS, EELS analysis showed that the actual ordered structure of the NT was not
46 oxidized (*vide infra*). The composition of the NTs was found to be invariable along its
47 length.
48
49
50
51

52 The atomic concentration of the relevant elements averaged over all samples can be used
53 to roughly estimate the stoichiometry of the MLC family. The average concentrations are
54 around 18 at% Ta, 22 at% La+Y and 60 at% S (**Fig. 2d**). This detailed analysis of several
55
56
57

NTs in each series suggests that the composition of MS-TX₂ is approximately (Y_xLa_{1-x}S)_{1.22}TaS₂, which is in line with the reported YS_{1.23}NbS₂ bulk structure.¹⁸ Formally the ratio between the two sulfides is calculated by the relation $2a_{\text{TaS}_2}/a_{\text{MS}}=1+y$ (where a is lattice constant of the binary compounds YS (LaS) and TaS₂). Using available data,^{23,24} the stoichiometry of the ternary MLC is calculated to be (YS)_{1.20}TaS₂ and (LaS)_{1.14}TaS₂. Obviously, the stoichiometry (1+y) of the quaternary (Y_xLa_{1-x}S)_{1+y}-TaS₂ MLCs varies along the composition tie line but the precise behaviour of this transition is not known.

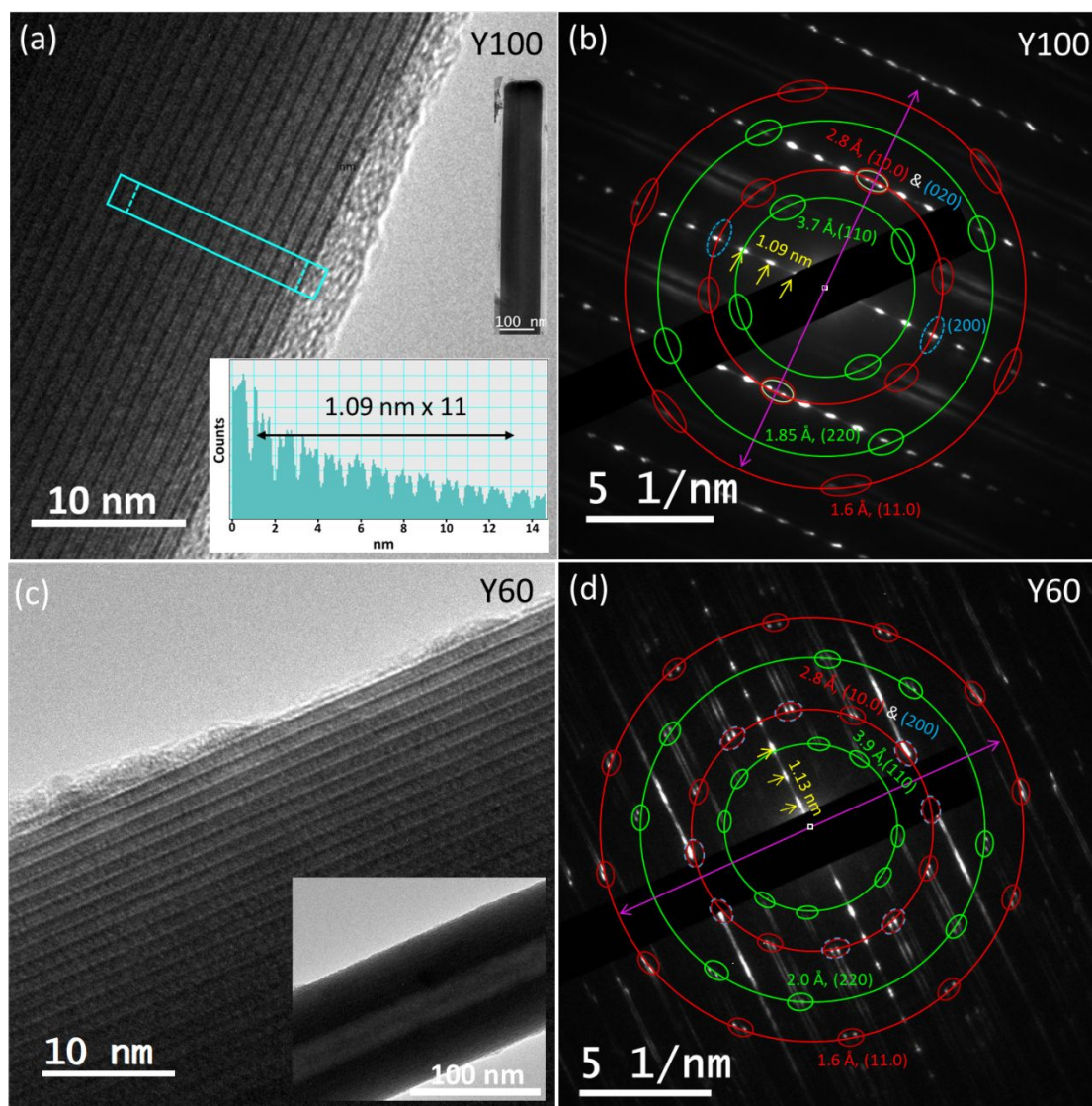


Figure 3. TEM images and corresponding SAED patterns of (a,b) YS-TaS₂ (Y100) and (c,d) La_{0.4}Y_{0.6}S-TaS₂ (Y60) misfit tubular structures with YS (or La_{0.4}Y_{0.6}S) and TaS₂ subunits periodically stacked along c -direction with the misfit along the a direction. Left panel (a, c) High-resolution and corresponding low magnification images with intensity line profile drawn perpendicular to the tubule axis showing the periodicity of the (Y,La)S and TaS₂ structures. (b, d) SAED patterns acquired from the NTs shown in the corresponding panels. Diffraction spots corresponding to the same interplanar spacings are

1
2
3 marked by circles (red for TaS₂ and green/blue for YS) and the respective Miller indices
4 are marked. The basal reflections are indicated by small yellow arrows and the tubule axis
5 is marked by purple double arrows. The chiral angles are 7.5° (b) and 3° (d).
6
7

8
9
10 Typical TEM images and the selected area electron diffraction (SAED) patterns of pure
11 YS-TaS₂ (Y100) are shown in **Fig. 3** and **Fig. S7**. The low magnification image of the NT
12 (inset of **Fig. 3a** and **S7a**) reveals a constant diameter of 120 nm along its entire length.
13 **Fig. 3a** shows the TEM image of the YS-TaS₂ superstructure, which is structurally
14 analogous to LaS-TaS₂ misfit structure. Here the YS and TaS₂ layers are stacked in
15 alternating sequence along their common *c* direction. The image clearly reveals that the
16 outermost layer of the ordered structure is TaS₂ (appearing as a dark line) and the
17 subsequent two planes belong to the YS slab. The intensity profile of this superstructure
18 (shown in the inset in **Fig. 3a**), indicates that the interlayer periodicity is 1.09 nm and this
19 value is consistent with the interlayer spacing found in other NTs (see **Fig. S7**). The NTs
20 exhibit a minor amorphous shell with varying sizes below 10 nm (**Fig. 3a&c, Fig. S7**),
21 which contains the main entities (Y(La),Ta,S) as well as carbon and is slightly oxidized.
22 The outermost layer is clearly recognizable as TaS₂, oxidation of the actual MLC layers
23 was successfully prevented (as proven by EELS, *vide infra*) by keeping the contact of the
24 NTs with air to the bare minimum.
25
26
27
28

29 The SAED patterns collected from the Y100 NTs are displayed in **Fig. 3b** (also see
30 **Fig. S7 c&d**). The intense and distinguished spots in the ED patterns indicate the good
31 crystallinity and ordered stacking of YS-TaS₂ layers in the NT. In **Fig. 3b**, the six pairs of
32 spots (marked by small red circles) with the interplanar spacing's of 1.6 and 2.8 Å are
33 azimuthally equally distributed (on the red circles) and are attributed to the (11.0) and
34 (10.0) planes of TaS₂. The four pairs of spots (marked by small green circles) with
35 interplanar distances of 3.7 Å and 1.85 Å are assigned to (110) and (220) reflections of the
36 rock-salt YS unit. The six-fold periodicity of the hexagonal TaS₂ and the four-fold
37 periodicity of rock-salt YS suggest that there is a single folding vector common for both
38 YS and TaS₂ units. This observation of a single periodicity was found for all (5) analyzed
39 NTs of pure YS-TaS₂. The basal plane reflections indicated by the small yellow arrows
40 show the periodicity of 1.09 nm along *c* direction, which is perpendicular to the tube axis
41 (marked by the purple double arrow). The 1.09 nm interlayer spacing is consistent with the
42 one determined from the intensity line profile of the TEM image (1.09 nm, see **Fig. 3a**).
43 Two pairs of YS (020) and TaS₂ (10.0) reflections (marked with small green and red
44 circles) are parallel to the tube axis. These spots reveal that the common commensurate *b*
45 axis coincides with the tube axis. The spots marked with the segmented small blue circles
46 along the basal plane correspond to the YS (200) plane (see **Fig. S7d** for a clear view) and
47 appear azimuthally rotated by 90° with respect to the (020) spots of YS. YS (020) and (200)
48 spots are approximately placed on the same circle and are perpendicular, which infers that
49 the *a* and *b* lattice parameters of YS can be considered equal. In general, the NTs exhibit a
50 high degree of crystallinity and the superstructure of MS-TaS₂ lattice is well preserved.
51
52
53
54
55
56
57
58
59
60

Both the stacking periodicity of 1.09 nm and the interplanar distances of the YS unit ($d_{110} = 3.7 \text{ \AA}$) are several pm smaller in comparison to LaS-TaS₂ (1.15 nm / 3.99 Å). This decrease of approximately 5-6% is consistent with the difference in the *a* lattice parameter between YS (0.549 nm) and LaS (0.581 nm)^{23,24} induced by the smaller ionic radius of Y³⁺ (90 pm) in comparison with La³⁺ (103 pm).²⁵ Indeed, this seems to have considerable influence in the rock-salt lattice and then, on charge transfer and interlayer spacing. The smaller periodicity of YS-TaS₂ compared to LaS-TaS₂ suggests that the interlayer interactions in the former are stronger leading to more closed packing of the YS and TaS₂ layers along the *c* direction. This view is confirmed by the DFT calculations and the Raman and FTIR results (*vide infra*).

In one of the YS-TaS₂ NTs analyzed here, a stacking disorder of YS and TaS₂ layers along *c*-direction was observed and is shown in **Fig. S8**. This kind of disorder has already been met earlier in MS-TaS₂ nanotubes.⁷

TEM images and the corresponding SAED pattern of Y_xLa_{1-x}S-TaS₂ NTs are shown in **Fig. 3c & d** (*x*=0.6) and in **Fig. S9** (*x*=0.9 and 0.2). The NTs exhibit very good crystallinity irrespective of the Y content. **Fig. 3d** shows a set of twelve (11.0) and (10.0) spots of the TaS₂ lattice and a set of eight (110) and (220) spots of the rock-salt Y_xLa_{1-x}S lattice, suggesting the existence of two folding vectors in the same NT.⁷ The multiplicity of these azimuthally equally distributed 12 couples of spots is six. Hence these two sets are azimuthally rotated by 30°, indicating two folding vectors for the TaS₂. Similarly, the quartets of (110) and (220) spots of Y_xLa_{1-x}S (eight couples), indicate two folding vectors for the YS layers. Two folding vectors were also found for most of the NTs with different Y contents (*e.g.* Y90, **Fig. S9a**). One of the NTs of the Y20 sample showed two folding vectors for the TaS₂ subunit but three folding vectors for the Y_xLa_{1-x}S layers, with the (200) reflections of all Y_xLa_{1-x}S orientations coinciding with (10.0) spots of TaS₂ (**Fig. S9b**). The relative orientation of the different layers of MS and TaS₂ subunits has been discussed in the case of LaS-TaS₂.⁷

An analysis of the interplanar distances of both, MS and TaS₂, subunits for different samples (see **Table S1**) reveals that while the Y_xLa_{1-x}S lattice is shrinking with increasing *x*, the TaS₂ lattice retains its structure irrespective of the Y content. The (11.0) and (10.0) reflections of the TaS₂ subunit are always found at 1.6 and 2.8 Å, respectively, whereas the reflections attributed to the Y_xLa_{1-x}S lattice are located at decreasing spatial frequencies with increasing Y content. The (110) interplanar distance decreases from 3.99 Å¹⁸ (*x*=0) to 3.9 Å (*x*=0.2 and 0.6, **Fig. S9b & 3d**), 3.8 Å (*x*=0.9, **Fig. S9a**) and finally to 3.7 Å (*x*=1, **Fig. 3b**). This homogeneous decrease in the MS unit goes in hand with the stacking periodicity that shows a similar behavior changing from 1.15 nm (*x*=0) to 1.09 nm (*x*=1) (**Table S1**). These changes correspond also to the deviation from stoichiometry 1.14 for the pure La-based MLC and 1.2 in the case of yttrium. Complementary X-ray diffraction (XRD) patterns were obtained for the MLCs (NTs and platelets) in order to confirm these structural changes. The results of these analyses are displayed in **Figure S10**. The shift of the stacking periodicity is clearly revealed and is confirmed by the major

reflections of the sublattices. The chiral angle of the NTs was found to vary between 3° and 8° . No statistically relevant dependence of the chiral angle on the Y-content of the NT was observed.

Atomic-scale structure and composition analyses

High-resolution (HR)STEM analysis of the NTs is displayed in **Fig. 4**, which shows typical images for different NTs acquired using the high-angle annular dark field (HAADF) detector. Additional HRSTEM images can be found in **Fig. S11 & S12**. **Fig. 4a** reveals the homogeneous contrast of all layered stacks of a pure yttrium-based MLC, *i.e.* Y100 NT. The atomic columns of the single layers of TaS_2 appear brighter than the double layers of Y(La)S due to the difference in atomic number Z ($Z_{\text{Ta}}=73$, $Z_{\text{Y}}=39$, $Z_{\text{La}}=57$) and the fact that the intensity in HAADF images goes approximately with $Z^{1.7}$.^{26,27} Evidently, the pair of YS and TaS_2 layers are coupled together and maintain a single orientation with respect to each other. This notion is confirmed by the observed projections along the $[200]$ and the $[10.0]$ (0.28 nm interatomic distance) direction of the respective layers, whose reflections overlap in the ED pattern (**Fig. 4a & 3b**).

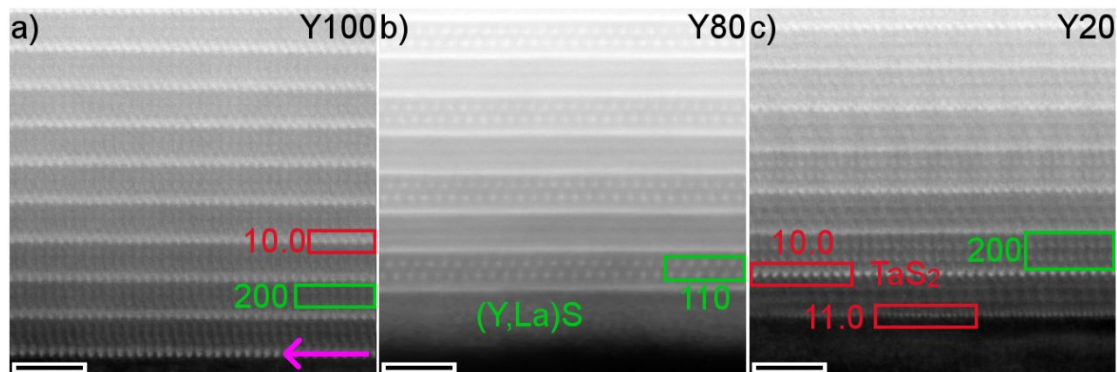


Figure 4. HAADF-STEM images of NTs from samples Y100 (a), Y80 (b) and Y20 (c). (a) The homogeneous contrast of the layers is in line with the single folding vector found by ED of the Y100 samples. (b, c) In contrast to (a), the appearance of the layer stack alternates along the c -axis, which is consistent with the ED patterns of such NTs revealing two folding vectors rotated by 30° with respect to each other. Identified projections of the different layers are marked in green and red for the $(\text{La},\text{Y})\text{S}$ and the TaS_2 subunits, respectively. The tube axis direction is indicated by the purple arrow. The appearance of the different projections agrees with the schematics in **Fig. 1**. Scale bars are 2 nm.

Contrary to the symmetric stacking of the layers with a single orientation in the Y0 and Y100 NTs, all other samples showed a rotation of the TaS_2 and the $(\text{La},\text{Y})\text{S}$ layers (**Fig. 4b&c, Fig. S11 & S12**). ED results suggest that there exist two folding vectors for both subunits, which are rotated by 30° with respect to each other. This angle is confirmed by the image of a NT from the Y20 sample displayed in **Fig. 4c**. The different orientations of TaS_2 in this NT can be linked to the $[10.0]$ and $[11.0]$ directions of TaS_2 by measuring the interatomic distances (0.28 and 0.16 nm). As these reflections encompass an angle of

30°, the adjacent layers of TaS₂ are rotated by 30° with respect to each other as expected from the ED results. As the multiplicity of the MS subsystem is four, only one of the layers of the (La,Y)S subunit coincides with a low-index zone-axis. The (La,Y)S layer that is stacked to the TaS₂ layer oriented in [10.0] direction can be identified as projection along [200] (**Fig. 4c**), similar to the case of the Y100 NT (**Fig. 4a**). While the two different orientations of the NT tend to alternate along the common *c*-axis leading to a double periodicity (**Fig. 4b&c**, **Fig. S11a&b**), **Fig. S11c&d** and **Fig. S12c &d** show that this (double periodicity) must not necessarily be the case for all the NTs. Furthermore, a disordered stacking was observed in a NT from the Y40 sample (**Fig. S12a &b**), in which two layers of TaS₂ appeared next to each other.

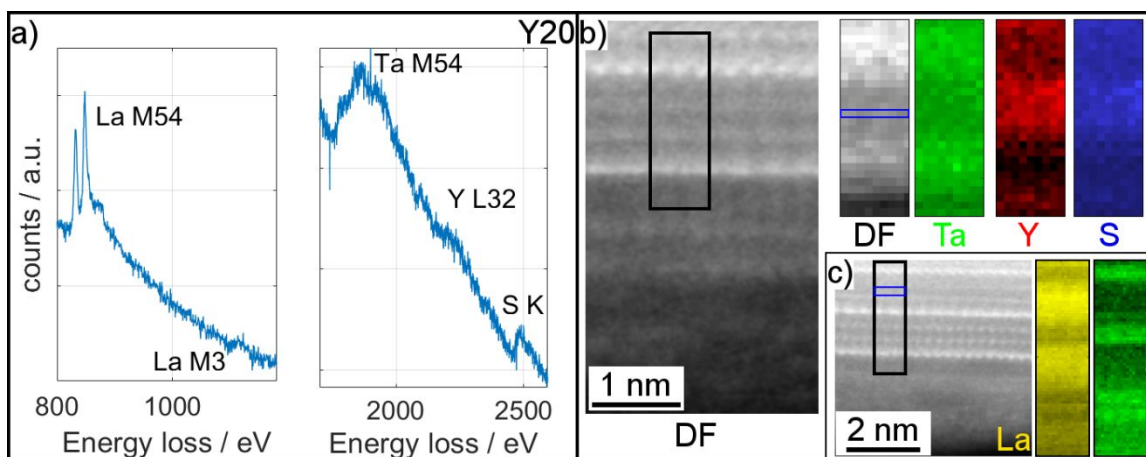


Figure 5: EELS analysis of a NT from sample Y20. (a) Spectra of the La M-edge as well as the Ta-M, Y-L and S-K edges are taken from regions marked blue in the dark field (DF) images in b and c, respectively. (b) Ta and Y are spatially separated between the different layers recognized in the DF image. (c) The La spectrum image obtained on the same NT shows enrichment of La in the two layers of MS.

The analysis presented so far suggests that La was uniformly replaced by Y in the entire volume of the investigated NTs. Results from STEM-EELS experiments on the Y20 sample conducted to ensure the in-phase replacement of La by Y are presented in **Fig. 5**. The depicted spectrum-image (SI) analyses of the NT reveal that both the La and Y distributions show a clear enrichment in the area identified as (La,Y)S double layer in the corresponding STEM-DF image (**Fig. 5b&c**). In contrast, the Ta concentration is increased in the layers, which appear brighter in the corresponding STEM image. This result is in accordance with the higher contrast expected from Ta ($Z=73$) with respect to La ($Z=57$) and Y ($Z=39$). Example spectra of the edges used for the SI analysis are shown in **Fig. 5a**, which includes the La-M edge (832 eV), the Ta-M (1735 eV), the Y-L edge (2080 eV) and the S-K edge (2472 eV). A comparison of three EELS spectra obtained from the (La,Y)S subsystem in Y100, Y60 and Y20 NTs is shown in **Fig. S13**. The spectra have been normalized in the region before the Y-L edge located at 2080 eV to visualize the increasing intensity in the Y-L edge. Additional EELS SI analyses conducted on the Y20, Y60 and

the Y100 are shown in **Fig. S14-S16**. These results present the same spatial separation of (La,Y) and Ta between the two subunits. The spectra taken from the amorphous shell of an Y20 NT (**Fig. S14b**) and the edge of an Y60 NT (**Fig. S15a**) clearly show the absence of oxygen and thus the successful prevention of oxidation of the NTs achieved by avoiding prolonged contact with air. The amorphous shell of the NTs consists of the main entities as well as carbon and a minor amount of oxygen (**Fig. S14b**). The stability of the NTs under the high electron doses necessary for the EELS experiments was found to decrease with increasing Y content (see **Fig. S16**).

Raman analyses

Raman analyses of lanthanide-based MLCs and their NTs were reported earlier.^{7,21,28} The features in the Raman modes of these NTs can be divided into two spectral regions. The low frequency modes from 100 to 200 cm^{-1} correspond to the phonon modes of the rock-salt (LnS) sublattice and the phonon modes above 250 cm^{-1} originate from the TaS₂ hexagonal sublattice.²⁸ The rock-salt unit (LnS) exhibits two stretching lattice phonon modes A_{1g} at ~ 120 and ~ 150 cm^{-1} designated as RSI and RSII modes, respectively. The frequency of both modes shifts downwards in energy with an increase in the mass of the rare earth element.²⁸ The RSI mode depends on the mass of Ln and S atoms ($M_{\text{Ln}}+M_{\text{S}}$), whereas the frequency of RSII mode depends on the effective mass ($\mu_{\text{eff}}=M_{\text{Ln}}\times M_{\text{S}}/M_{\text{Ln}}+M_{\text{S}}$). It is also noted that the metal atom in the TS₂ layer influences the frequency of RSI and RSII modes as observed in the case of LaS-TaS₂ and LaS-NbS₂.^{21,28} The charge transfer influences the intralayer and interlayer interactions within the MLC lattices.²⁸ The modes corresponding to TS₂ unit, especially the E_{2g} mode is affected by the charge transfer from the MS to the TS₂ unit.^{28,29}

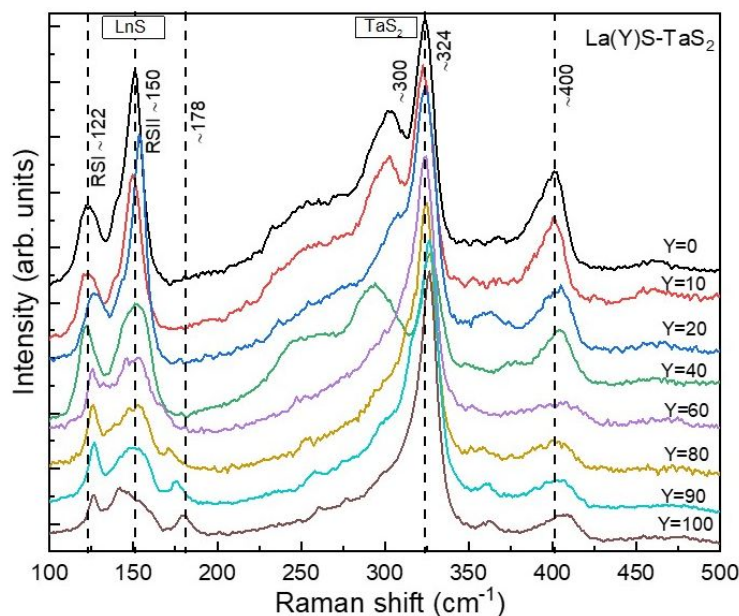


Figure 6. Raman spectra of individual Y_xLa_{1-x}S-TaS₂ (x=0 to 1) NTs recorded using 633 nm laser excitation and 600 grooves/mm grating in backscattering geometry. The vertical dotted lines show the major phonon modes related to the LnS and TaS₂ subunits.

1
2
3
4
5 Raman measurements of pure YS-TaS₂ and (Y_xLa_{1-x}S)_{1+y}TaS₂ (x=0 to 0.9) were carried out
6 with individual NTs in the range 100 to 500 cm⁻¹ using 633 nm laser light and are shown
7 in **Fig. 6** (see also **Fig. S17a** collected using 1800 grooves/mm). Despite the large mass
8 difference between La (139u) and Y (89u), the Raman features of YS-TaS₂ tubular crystals
9 and its alloys are quite similar to their LaS-TaS₂ counterparts except for some
10 dissimilarities in YS lattice modes. However, no previous literature data is available for
11 YS structures and YS-TaS₂ MLCs.
12
13

14 Regarding the low frequency range, the samples can be divided into two categories, namely
15 Y contents below and above 40%. While for the Y10 and Y20 samples the Raman features
16 follow the separation in RSI and RSII modes observed for the LaS-TaS₂ NTs, the spectrum
17 appears significantly different for NTs with Y contents >40%. In this range, a sharp peak
18 around ~125 cm⁻¹ is seen, which is almost invariant with the Y content. In addition, instead
19 of the sharp peak of the RSII mode in LaS-TaS₂, a broad arrangement of overlapping peaks
20 around 150 cm⁻¹ can be observed whose intensity is lower and varying with the Y content.
21 Moreover, a peak at 178 cm⁻¹ appears for YS-TaS₂, which shifts downwards with reducing
22 Y content. This particular signal is not seen in the pure LaS-TaS₂, nor in other MLC NTs
23 of the rare-earth atoms.^{7,30}
24
25
26

27 To understand further the origin of these peaks, Raman spectra with different laser
28 excitation energies (532, 633 and 785 nm) have been acquired (**Figs. S17** and **S18**).
29 **Fig. S17b** shows the overlay of the Raman spectra of individual NTs with increasing Y
30 content collected using 785 nm laser excitation. The accuracy of these measurements is
31 higher since the spectra presented here are the average of several acquisitions, collected
32 using 1800 grooves/mm grating. Furthermore, this laser excitation penetrates deeper into
33 the NT core, thereby reducing the influence of the NT surface. The peak observed at
34 178 cm⁻¹ appears to be very prominent with the 785 nm laser excitation and it gradually
35 shifts downwards with decreasing Y content. The broad peak at 150 cm⁻¹ almost diminishes
36 in YS-TaS₂.
37
38
39

40 A clear assignment of these low-frequency modes observed for Y contents higher than 40%
41 is not possible without deeper analysis and theoretical support, which lies outside the scope
42 of this work. Yet one can discuss the differences with respect to previously reported MLC
43 structures and give possible explanations. The Raman modes are influenced by a number
44 of properties including the changing atomic mass, the observed structural variation and the
45 charge transfer from the MS to the TaS₂ unit. Y is by far the lightest atom so far
46 encountered in the MS unit of MLCs and the appearance of modes at higher energies
47 generally agrees with the expected shift due to the reduced mass of the Y atom. However,
48 an estimation of the shift of the RSI and RSII modes based on their dependence on the
49 mass and effective mass, respectively,²⁸ yields energies of 145 cm⁻¹ (RSI) and 156 cm⁻¹
50 (RSII) for YS-TaS₂, which disagrees with the experimental data preventing thereby a clear
51 assignment of the observed peaks.
52
53
54
55
56
57
58
59
60

1
2
3 In addition to the mass change, the observed structural change of the MLC NTs will affect
4 the Raman response. The decreasing *c*-axis periodicity of the for YS-TaS₂ (1.09 nm)
5 compared to LaS-TaS₂ (1.15 nm), concluded from the TEM/ED studies, leads to a closer
6 packing of the lattice, in which case stronger interlayer interactions can be expected. In
7 addition, the theoretically expected stoichiometry of (YS)_{1.2}-TaS₂ could possibly lead to a
8 supercell along the misfit *a*-direction composed of six unit cells of YS and five unit cells
9 of TaS₂ (consider **Fig. 1e**). In such a supercell, specific sites in the MS unit could vary
10 energetically and favor the occupation with either La or Y atoms leading to possible
11 additional Raman modes. In the alloys (Y_xLa_{1-x}S-TaS₂), the lattice consists of both LaS and
12 YS units in different proportions based on the composition. Though both crystallize in the
13 rock-salt lattice, they have different '*a*' lattice parameters (LaS *a*=5.81 Å and YS *a*=5.49
14 Å),^{23,24} which causes small lattice distortions in the mixed lattice. Given the fact that each
15 sulfur atom has six nearest neighbor metal atoms, the local environment may vary for say
16 pure six La atoms or four La and two Y atoms, *etc.* Hence the rock-salt unit is expected to
17 have more than one kind of local vibration. Additionally, the ED and HRTEM of the NTs
18 with mixed La and Y composition showed two distinct orientations, instead of the one
19 orientation in the ternary MLC, at least for the outermost layers. On the other hand, the
20 pure LaS-TaS₂ and YS-TaS₂ tubes exhibit single orientation. The low-frequency Raman
21 peaks of LaS-TaS₂ are relatively sharp, compared with the mixed tubes at low Y content.

22
23
24
25
26
27 The structural modulation and the valence shell configuration of the rare-earth atom in the
28 rock-salt unit vastly affects the Raman modes of the LnS unit.³¹ Previously, NTs from
29 mixed rare-earth lattices Ln_xLa_(1-x)S-TaS₂ (Ln=Pr, Sm, Ho, Yb) were prepared and
30 analyzed *via* Raman spectroscopy³¹. The Raman modes (A_{1g}) of the rock-salt unit of the
31 mixed tubes exhibited a blue shift and splitting into two peaks in the case of an electronic
32 structure with open 4*f*-shell (Pr, Sm, Ho) (mixed with La atom). On the other hand, the
33 Raman modes of the rock-salt lattice of a closed 4*f*-shell (Yb) atom revealed a red shift in
34 comparison with the pure LaS-TaS₂ nanotubes. In the present case replacing La by Y, both
35 atoms have the same number of valence electrons, however, in contrast to the La atom,
36 yttrium does not possess any vacant *f*-orbitals, which could influence the Raman signals of
37 the two compounds. Additionally, an alteration in the charge transfer is expected, which
38 could also influence the YS phonon modes. Furthermore, we cannot exclude a contribution
39 from the TaS₂ unit to the low frequency range.^{7,32} In summary, a vast number of effects
40 plays into the existence of Raman peaks in the low frequency range for MLC-NTs
41 Y_xLa_{1-x}S-TaS₂, which requires further (theoretical) studies to allow a clear assignment of
42 the modes. Especially polarization-dependence Raman measurements could also help
43 further elucidating the complex Raman signature of the rock-salt sub-lattice of the MLC
44 alloys.

45
46
47
48
49
50 The phonon modes around 250 to 300 cm⁻¹ of LaS-TaS₂ NTs are very broad and weaker.
51 The assignment of these modes is debatable and they are attributed to nonlinear Raman
52 transitions or transitions associated with defects. These phonon modes gradually
53 disappeared as La was replaced by Y. On the other hand, the Y rich NTs (> Y40) show a
54
55
56
57

1
2
3 tiny peak around 260 cm^{-1} , which downshifts with decreasing Y content. This peak may be
4 the manifestation of the nonlinear Raman transition related to the YS-TaS₂ structure.²⁸
5

6 The Raman mode observed at 324 cm^{-1} corresponds to the E_{2g} mode of TaS₂, the large shift
7 in this mode compared to bulk TaS₂ flakes (280 cm^{-1}) was ascribed to charge transfer from
8 LaS to the TaS₂.^{28,29} In the present case, this mode is marginally shifted to higher energies
9 on replacing La by Y, which could be explained by a slightly modified charge transfer from
10 the YS to TaS₂ in comparison with LaS to the TaS₂. The 400 cm^{-1} peak was assigned to the
11 out-of-plane A_{1g} mode of TaS₂.²⁸ This sublattice is only weakly influenced by the Y to La
12 exchange, indeed this peak shows some broadening and little shift, if any replacing La
13 by Y. The modes above 600 cm^{-1} are characteristics of oxidation products of MLC. In the
14 present measurement, no oxidation of the NTs occurred during acquisition, though the
15 tubes were exposed for an extended time (40 min) to the laser irradiation. The Raman
16 spectra recorded on different NTs of the same MLC compound show similar features
17 (Fig. S19), indicating that the Raman measurements are very reproducible.
18
19
20
21

22 FTIR measurements

23 The normalized FTIR spectra of different (Y_xLa_{1-x})S-TaS₂ compounds are displayed
24 in Fig. 7. The spectra show transmissivity in the range of about 1000 to 6000 cm^{-1} for all
25 compounds under study with a decreasing signal-to-noise ratio upon reaching higher wave
26 numbers. Pure TaS₂ powder did not show any signal in this range, due to the high free-
27 carrier concentration, *i.e.* absorption energy beyond 6000 cm^{-1} , which agrees with previous
28 results.³³ The measured FTIR spectra clearly show that for Y contents larger than 20%, the
29 maximum transmission exhibits considerable shifts to lower energies with increasing Y
30 content. Furthermore, at high Y content the transmission spectra exhibit two nearby
31 maxima with a tiny dip in between. The source of this splitting is not clear, suggesting two
32 populations with different free-carrier densities. The reduced transmission in the lower
33 energy range ($<3000\text{ cm}^{-1}$) is associated with free-carrier effects. In addition, the
34 absorption in the higher energy region (less transmission) is associated with interband
35 transitions.
36
37
38
39

40 The IR reflectivity of several MLCs was measured in the past.^{34–36} The reflectivity
41 threshold was attributed to the plasmon resonance of the free carriers in the misfit structure.
42 The spectra were fitted with the Drude-Lorentz model assuming a constant effective mass
43 of $1.0 m_0$ as described in the respective section in the SI (attempts to fit the data to a pure
44 Drude model alone were not successful).^{37,35} In this model, the rock-salt unit MS is
45 described by a Lorentzian (localized) oscillator, which contributes an electron to the Fermi
46 sea of the free carriers in the hexagonal TS₂ unit. On the other hand, the semimetallic
47 character of the TS₂ unit in the MLC with a half-filled $5d_{z^2}$ band is well described by free
48 electrons, *i.e.* the Drude model. In addition, the plasma frequency calculated from the
49 position of the maximum in the transmission spectra (equation S5) can be used to estimate
50 the carrier concentration and the charge transfer from MS to the TS₂ unit in the MLC
51 compounds.³³
52
53
54
55
56
57
58
59
60

Using the Drude-Lorentz model and the plasma frequency, the free carrier density in the TaS₂ layer and the amount of charge transfer from the MS to the TS₂ unit were calculated. Overall, the carrier density and thus the number of carriers per Ta atom goes down with increasing Y content for both approaches (**Fig. 7b** and **Table S2**) although in a non-uniform fashion. This change in the carrier density can be attributed to a modified charge transfer from the MS to the TS₂ unit. Alternatively, structural changes induced by the substitution of La by Y could induce these changes. This important point requires further investigation in future studies. Noticeably, the fitting of the Drude-Lorentz model to the lower energy part of the spectra for high-Y MLCs is not as good as for the ones with low Y content.

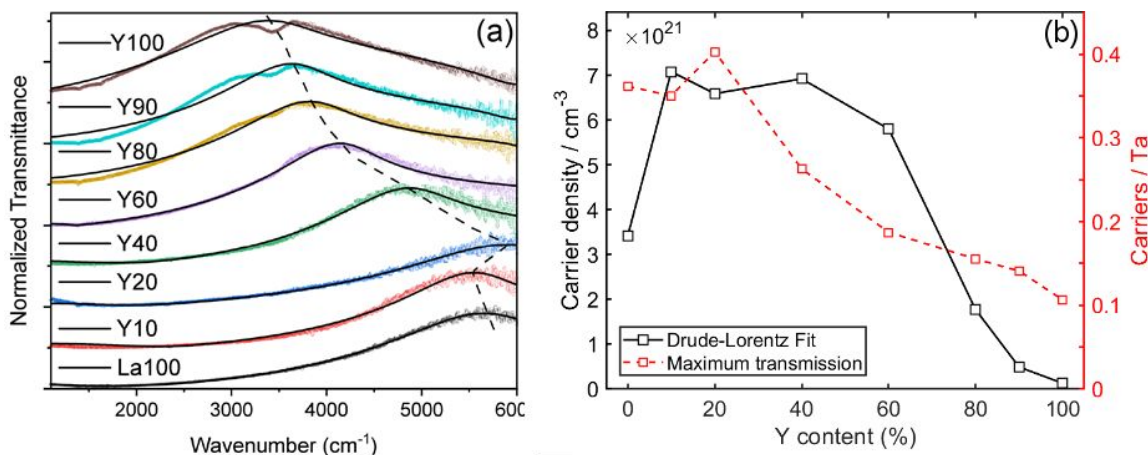


Figure 7: (a) Normalized transmission spectra of $(Y_xLa_{1-x})S-TaS_2$ compounds with varying Y proportions. The solid lines represent the fitted Drude-Lorentz model. The dashed line (guide to the eye) indicates the non-linear shift of the transmittance in the spectra. (b) The variation of carrier density and Carriers per Ta atom calculated from the Drude-Lorentz model (black curve) and using equation S5 (dashed red curve) as a function of Y % in the $(Y_xLa_{1-x})S-TaS_2$ misfit compound.

The rise in the free carrier density for Y10-Y40 obtained by fitting the Drude-Lorentz model (black line in **Fig. 7b**) might result from a variation in the composition and structure of the $(Y_xLa_{1-x})S-TaS_2$ MLC alloy that has occurred in this range. In fact, according to the EDS analyses of the NTs, the Y10 and Y20 samples were found to contain a reduced percentage of Y. For higher percentages of Y, the measured Y content corresponds with the formal content in the alloy. One possible explanation for this non-uniform behavior is that the stoichiometry of the alloy does not change continuously from 1.14 $((LaS)_{1.14}TaS_2)$ to 1.20 $((YS)_{1.20}TaS_2)$.

We are aware of the ambiguity of the fitting procedure caused by a probable change of the effective mass of the carrier upon variation of the Y content in the MLC. Nevertheless, the trend of a decreasing carrier density in the TaS₂ unit with increasing Y content is evident. A similar dependence of the plasma frequency on the Y content is observed in STEM-EELS measurement of the bulk plasmon (details see SI, **Fig. S20**). The determined energy

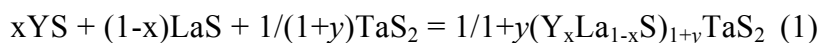
of the bulk plasmon decreases from 29.3 eV (TaS₂) to 27.7 eV ((La_{0.8}Y_{0.2}S)-TaS₂) and 23.3 eV (YS-TaS₂) qualitatively indicating the same trend of the free carrier density in the TaS₂ slab and the charge transfer between MS and TaS₂ unit.

In order to further investigate the electrical properties of the NTs, electrical measurements of single Y10 NTs in a dual-beam instrument (**Fig. S21&S22**) were conducted. The NTs were found to be semimetallic and exhibit a conductivity in the range of 10⁴-10⁵ Sm⁻¹, which coincides with values obtained from bulk material of comparable MLCs.³⁴

In summary, the experimental results from FTIR, Raman and EELS analysis as well as the DFT calculations (*vide infra*) suggest that the charge transfer is modified by replacing La with Y. As the DFT results indicate a complex dependence of the charge carrier redistribution upon charge transfer modification, we can only speculate on the nature of the actual variation of the charge transfer from the MS to the TaS₂ unit. Nevertheless, the experimental results show that the (partial) substitution of La by Y provides a fine control over the plasmonic and vibrational properties of the NTs, which could be relevant for IR-based plasmonics using 1D devices.

Computational results

Substitutional replacement of La by Y should lead to a change in the lattice parameter of the metal sulfide (MS) and, consequently, to a variation in the commensurability between the MS and the TaS₂ layers. DFT calculations were employed to trace a possible equilibrium between different (Y_xLa_{1-x}S)_{1+y}TaS₂ misfits as well as the competition between a misfit and the corresponding binary sulfides. Therefore, conveniently for both purposes the course of the enthalpy change ΔH was analyzed for the model reaction:



ΔH was estimated as the difference in total energies between the products and the reactants, where the compounds have been considered in their solid states. According to the calculations, an increase in the yttrium content (index x) within the (Y_xLa_{1-x}S)_yTaS₂ misfit should enhance the relative content of the MS unit, increasing the incommensurability index y (**Fig. 8**). Particularly, the compositions (LaS)_{1.14}TaS₂ and (YS)_{1.20}TaS₂ are found as the most favorite ones among the considered ternary misfits. These findings are consistent with the experimental analysis presented above. Varying the composition (x) of the rare-earth parts within the quaternary misfits yields an almost linear variation in the relative stability for a given value of y. The dependence of ΔH on x shows different slopes for different values of the parameter y, which can have cross-points. A gradual transition from (Y_xLa_{1-x}S)_{1.14}TaS₂ to (Y_xLa_{1-x}S)_{1.20}TaS₂ can be expected over a wide range of x = 0.2-0.5 assuming a random distribution of the RE atoms. Leaving alone the entropy factor, a regular distribution of the RE atoms like in-plane or strip-like orderings within the (Y_{0.5}La_{0.5})-part has little influence on ΔH, contributing about 0.01 to 0.02 eV/RE-atom, respectively. Therefore, the additional entropy of mixing would favor random distribution of the RE elements in the MS lattice.

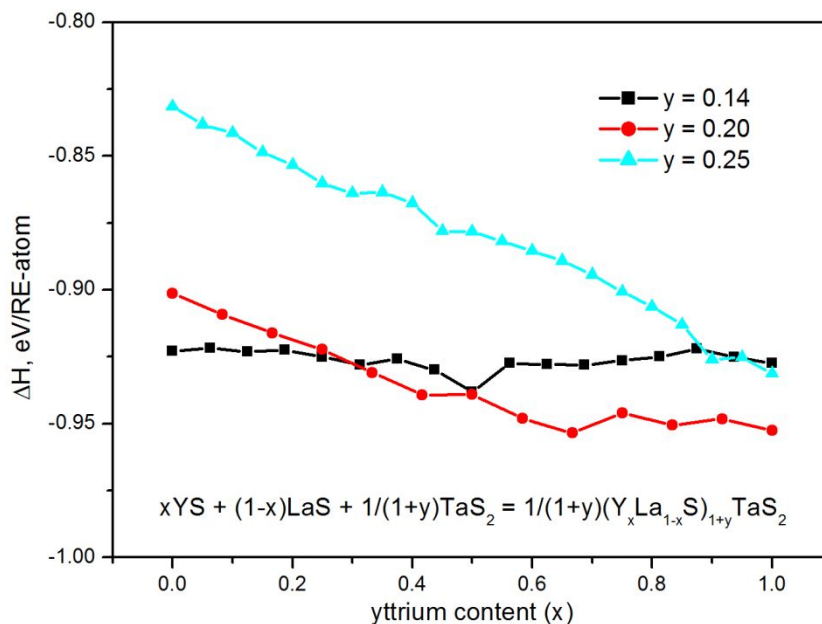


Figure 8. DFT calculation of the enthalpies of formation ΔH from binary sulfides for three misfit approximants $(Y_xLa_{1-x}S)_{1+y}TaS_2$, depending on the incommensurability factor (y) and yttrium content (x). A positive value ΔH corresponds to endothermic reaction.

According to the calculations, all studied $(Y_xLa_{1-x}S)_{1+y}TaS_2$ misfits should have metal-like properties. The calculated electronic densities-of-states (DOS) are plotted in **Fig. 9** for ternary and several quaternary compounds, unveiling a close similarity in the distribution of electronic states between the different MLC compounds. The $S3p$ - and REd -states responsible for the covalent RE-S bonding within MS slabs are found in the wide valence band below -1.5 eV relative to the Fermi level E_F . The band of $S3p$ -states responsible for covalent Ta-S bonding within the TaS_2 layers is found in the same energy region. In addition, the TaS_2 layers induce the band of localized $Ta5d_{z^2}$ -states just below E_F . This localized $Ta5d$ -band being half-occupied in pristine 2H- TaS_2 becomes fully or almost fully occupied in the $(Y_xLa_{1-x}S)_{1+y}TaS_2$ misfits, reflecting a charge transfer from the donating $(Y_xLa_{1-x}S)$ slabs to the accepting TaS_2 layers.

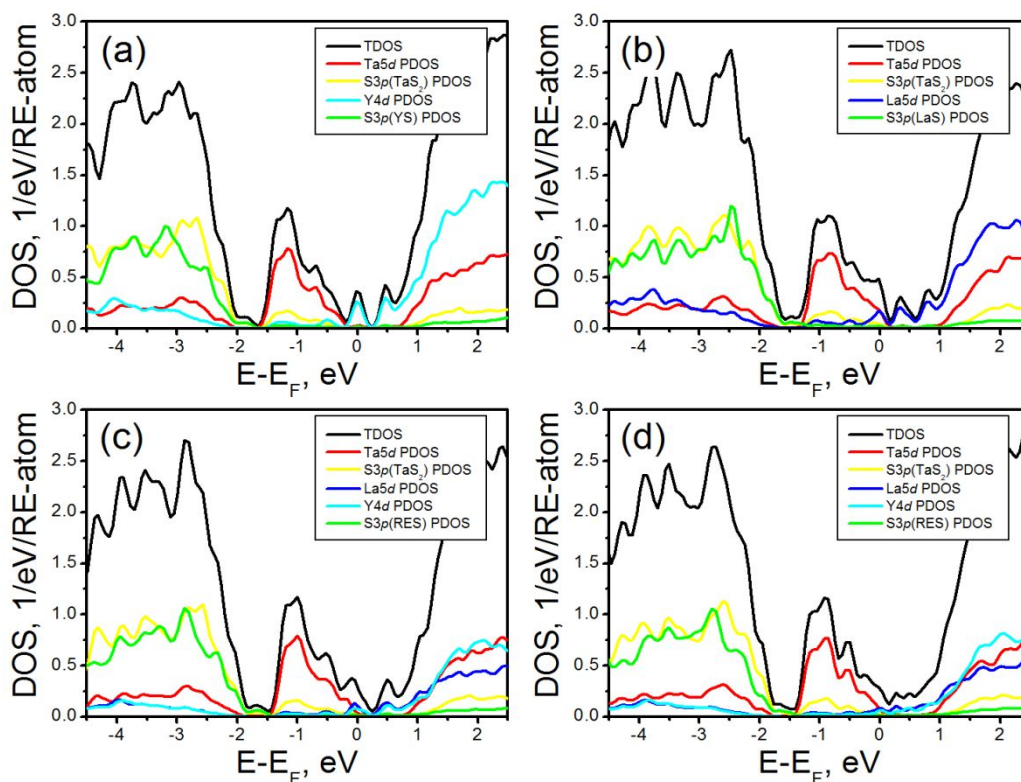


Figure 9. Electronic densities-of-states (DOS) for the misfits: a) $(YS)_{1.20}TaS_2$, b) $(LaS)_{1.14}TaS_2$, c) $(Y_{0.5}La_{0.5}S)_{1.20}TaS_2$, and d) $(Y_{0.5}La_{0.5}S)_{1.14}TaS_2$ obtained from DFT calculations.

In general, the DOS profiles of the studied MLC resemble a close similarity irrespective of the composition. The calculations furthermore provide evidence for a minor influence of the type of RE-element in $(Y_xLa_{1-x}S)_{1+y}TaS_2$ on the occupation of the $Ta5d_{z^2}$ -band, which is found almost fully occupied in comparison to that in isolated TaS_2 layer. Indeed, the formation enthalpies ΔH of these misfits at a given y do not demonstrate extreme points and their functions on the composition x are smooth (**Fig. 8**). However, the origin of the metallic properties in the studied misfits can have a qualitative difference depending on the ratio between the MS and TaS_2 parts, *i.e.* the incommensurability factor y . It plays a major role in the position of E_F , hence, predetermining the lattice stability and the chemical reactivity of a misfit. Particularly, at $1+y = 1.14$ the Fermi level is hosted mostly by the $Ta5d_{z^2}$ - and $S3p$ -states from the TaS_2 layer (**Fig. 9b** and **9d**). Hence, such misfit could demonstrate an electrophilic character or a minor S-deficiency, *i.e.* excess electrons which fill the $Ta5d_{z^2}$ -band. At higher $1+y = 1.20$, the Fermi level shifts to a higher energy and can be found away from the $Ta5d_{z^2}$ -band, and the density of $S3p$ -states gets lower until its full suppression (**Fig. 9a** and **9c**). Here, the main contribution to the Fermi level comes from a shallow d -band of the RE-elements. Hence, in order to obtain E_F at a local DOS minimum

such misfit could act in chemical reactions both roles either as nucleophilic or electrophilic agent (reducer or oxidizer).

Fig. 8 shows that the most stable stoichiometry of the MLC lattice for lanthanum-rich alloys is the $1+y=1.14$. Indeed, the MLC lattice is not favorable for substitution of extra Y^{3+} , which are smaller (ionic radius of 90 pm compared to 103 pm for the La^{3+})²⁶ and more electronegative than the lanthanum atom. For yttrium concentrations above $x=0.3$ the calculations show that the lattice with a stoichiometry $1+y=1.20$ becomes more stable than the 1.14 lattice. Indeed, the EDS analyses (see **Fig. 2d**) show that the yttrium concentration up to $x=0.2$ is substoichiometric, *i.e.* it does not follow the amount of added yttrium in the precursor. According to these analyses, the yttrium concentration in the NTs increases proportionally to the amount of added yttrium in the precursor at $x=0.3$, which agrees with the calculations presented in **Fig. 8**.

Obviously, the MS slabs within $(Y_xLa_{1-x}S)_{1.14}TaS_2$ misfits possess already the number of electrons exceeding the storage capacity of the TaS_2 layers. A further increase of y and, correspondingly, the shift of E_F into the high DOS of the conduction band would destabilize the misfit lattice. Extremely large y values could be achieved for a misfit based on MS slabs with a high atomic number per surface area, for example, using the ScS slabs. Preliminary DFT calculations on the stability of hypothetical $(ScS)_{1+y}TaS_2$ misfits suggest a minimum of ΔH at $1+y = 1.42$. Yet, it appears to be ~ 0.4 eV/RE-atom higher in energy, then that for known $(YS)_{1.20}TaS_2$ and $(LaS)_{1.14}TaS_2$ misfits. Consequently, the existence of pristine $(ScS)_{1+y}TaS_2$ or heavily Sc-doped $(Y_xLa_{1-x}S)_{1+y}TaS_2$ misfits is highly unlikely. Indeed, as reported above, attempts to synthesize the corresponding MLCs by the CVT method used for the synthesis of $(Sc_xLa_{1-x}S)_{1+y}TaS_2$ MLC and nanotubes thereof were unsuccessful.

A functional dependence of the calculated charge transfer from the MS slab to the TaS_2 layer can be registered depending on the Y content x (**Fig. S23**). In agreement with the electronegativities of the RE elements, the charge transfer diminishes gradually from a LaS-based misfit to its corresponding YS-counterpart. The RE atoms act as the main donors of electrons here: the effective charges on La and Y atoms (+0.40 e and +0.29 e) within the misfit lattice are found to be more positive by 0.12-0.14 e in comparison to the parent binary sulfides. The essential donation from the RE atoms can be proven also by adding vacancies in either the RE or S sublattice of the RE slab: a drastic drop of charge transfer is obtained already after introduction of single atom RE-vacancies, while the charge transfer remains insensitive to S-vacancies. Expectedly from the DOS picture (**Fig. 9**), the Ta atoms are the main acceptors of charge from the RE atoms: the charge on Ta atoms within the MLC is reduced to 0.4 e in comparison with +0.5 e within an isolated TaS_2 layer. Noteworthy, at any value of $(1+y)$ the number of Ta acceptors is smaller, than the number of RE donors, and the band of $Ta5d_z^2$ -states is (almost) fully occupied for any considered misfit structure. Therefore, in the studied MLCs, the S atoms of TaS_2 act as another repository of excessive electrons from RES, causing either an increase of electron

density at the interface RES||TaS₂ or even forming the dative bonding to the RE atoms at appropriate interatomic distances.¹⁹ Both Ta and S atoms within TaS₂ layer act as acceptors, yet, the mutual charge redistribution within TaS₂ layer is found to have a complex character. In general, the gradual replacement of La on more electronegative Y leads to an expected electronic depletion of the S atoms within the TaS₂ subunit and to a minor benefit in electrons at Ta atoms. Comparative analysis of the atomic charges on TaS₂ atoms within the misfits and within isolated TaS₂ layer confirms the charge saturation of Ta5d_{z²}-states within MLCs at any sort of studied RE atoms (**Fig. S23**). The electronic depletion of S(TaS₂) atoms with increasing Y-content has a more pronounced character, approaching the atomic state as observed in an isolated TaS₂ layer.

According to the DOS picture and the analysis of charge distribution, the content of holes from Ta5d_{z²}-states within (La,Y)S-TaS₂ misfits should be very low and almost invariant on Y-content. The excessive electrons hosted at the TaS₂ layer must be considered as the charge carriers within the studied MLCs, whose content should drop at increasing Y-content. The latter trend has indeed been confirmed by means of IR spectroscopy.

Conclusions

In this work, the family of misfit layered compounds (MLC) Y_xLa_{1-x}S-TaS₂ and nanotubes (NTs) thereof with different values of x (0 ≤ x ≤ 1) and alternating Y_xLa_{1-x}S and TaS₂ layers, were studied. They were prepared *via* the high-temperature chemical vapor transport (CVT) technique with TaCl₅ as the transporting agent. The Y_xLa_{1-x}S-TaS₂ nanotubes were studied experimentally using different electron microscopy techniques, Raman scattering and infrared transmission studies as well as theoretically by DFT calculations. It was found that the yttrium can occupy the lanthanum site in the MS sublattice at any value of x, but the overall concentration of the NTs in the product decreased with increasing x. Electron diffraction and HAADF-STEM analysis of pure YS-TaS₂ nanotubes showed that they exhibit a single orientation with the (commensurate) *b*-axis parallel to the axial growth axis of the NTs. In the quaternary Y_xLa_{1-x}S-TaS₂ tubes the layers mostly show two orientations rotated by 30° with respect to each other. In several cases, the nanotubes exhibited double periodicity, *i.e.* the adjacent Y_xLa_{1-x}S-TaS₂ layers showed a relative rotation of 30°. The Y_xLa_{1-x}S sublattice and the stacking periodicity along the *c*-axis was found to decrease homogeneously with increasing Y content going in hand with the smaller lattice constant of YS with respect to LaS.

A typical MLC Raman spectrum was observed for the NTs with low Y content with the two main peaks in the range of 100-150 cm⁻¹ characteristic for the MS lattice and in the range of 250-400 cm⁻¹ for the vibration modes of TaS₂. However, for x > 0.4 the Raman response changed significantly including the appearance of a peak at 178 cm⁻¹ for pure YS-TaS₂. Infrared measurements revealed transmissivity peaks of the studied material in the range of 1000 – 6000 cm⁻¹. The position of maximum transmission, and thus the plasmon

1
2
3 frequency, shifts to lower energies with increasing Y content. This shift is attributed to an
4 alteration of the free charge carrier density within the MLC.
5

6 DFT calculations indicate that the $Y_xLa_{1-x}S-TaS_2$ MLC are stable, while those of $Sc_xLa_{1-x}S-$
7 TaS_2 were found to be unstable. Indeed, attempts to obtain these latter MLC and NTs
8 thereof using the present method, were unsuccessful. The studied $Y_xLa_{1-x}S-TaS_2$ MLC NTs
9 were found to be semimetallic with an experimentally measured conductivity in the range
10 of 10^5 Sm^{-1} . The main contribution to the Fermi level comes from the Ta $5d$ band for low
11 x values and from the $4d$ Y and $5d$ La bands for higher values of x .
12
13

14 This study extends the range of known MLC compounds and NTs thereof. The present
15 results show that the structural, plasmonic and vibrational properties of the $Y_xLa_{1-x}S-TaS_2$
16 MLC can be tuned by variation of the Y content making them highly interesting for
17 applications, *e.g.* for plasmon technology in the IR range. Nevertheless, further
18 investigations are necessary to disentangle the complex interplay between microscopical
19 properties, *i.e.* microstructure and charge transfer, and the observed NT responses such as
20 the infrared transmission.
21
22
23

24 25 26 **Experimental/Methods**

27 *Synthesis of $Y_xLa_{1-x}S-TaS_2$ nanotubes*

28
29 YS-TaS₂ and $Y_xLa_{1-x}S-TaS_2$ NTs were prepared by the chemical vapor transport (CVT)
30 technique using evacuated quartz ampules following the well-established protocol for the
31 synthesis of modified LaS-TaS₂ NTs. The reactants were handled under the inert
32 atmosphere provided by a glovebox in order to prevent the oxidation of the precursors. A
33 stoichiometric amount of Y (Sigma-Aldrich 99.9%), Ta (Alfa Aesar 99.9%) and S (Sigma-
34 Aldrich 99.98%) was mixed in an agate mortar accordingly to the proportion 1:1:3 (19 mg
35 0.13 mmol of Y(La); 25 mg 0.13 mmol of Ta; and 13.2 mg 0.41 mmol of S). For Y_xLa_{1-}
36 $xS-TaS_2$ NTs, part of the Y was replaced by La (Strem Chemicals 99.9%) in a proportion
37 ranging from 10 at% to 90 at%. A small amount (2 mg) of TaCl₅ (Sigma-Aldrich 99.99%)
38 was used as a catalyst for the synthesis of nanotubular species. The ampule was connected
39 to a vacuum system equipped with a rotary pump and a diffusion pump protected by a
40 liquid N₂ trap. The quartz ampules were sealed under vacuum ($<1 \times 10^{-5}$ torr) and transferred
41 to a pre-heated vertical furnace for the annealing process. The annealing was performed in
42 two steps using two opposite gradients of temperature under constant monitoring of the
43 temperature inside the furnace. In the first step, the ampules were submitted to a thermal
44 gradient formed by 350 °C at the bottom edge and 800 °C at the upper edge. After 1h, the
45 ampules were moved inside the bore of the furnace and exposed to an opposite temperature
46 gradient between 857 °C at the bottom part and 400 °C at the upper part. After 6h of high-
47 temperature annealing, the ampules were withdrawn from the furnace and were allowed to
48 cool down to room temperature. As previously observed for modified LaS-TaS₂ nanotubes,
49 the mass transport was negligible and the products were accumulated in the lower (high-
50
51
52
53
54
55
56
57
58
59
60

1
2
3 temperature) edge of the ampule. The product was collected and stored in N₂ atmosphere
4 for further analysis.
5

6 *Characterization of the nanotubes*

7
8 Scanning electron microscopy (SEM) imaging was done with a Zeiss Sigma 500 model. A
9 minute quantity of native sample was picked up by a capillary tube and dispersed on carbon
10 tape for the SEM analysis. Energy dispersive X-ray spectroscopy (EDS) analysis was
11 performed with the Bruker XFlash/60mm retractable detector. The relative abundance
12 (yield) of the NT was estimated by analyzing many SEM images of the product. The
13 determined yields were based on the relative surface area occupied by the NTs compared
14 to the area occupied by the entire product in the SEM images. Each material was
15 synthesized three times and at least ten SEM images for each product were analyzed. While
16 being only semi-quantitative in nature, the overall yield did not vary appreciably from one
17 batch (of the same material) to the other and the relative abundance of the NTs for the
18 different Y_xLa_{1-x}S-TaS₂ materials was found to be reproducible.
19
20
21

22 Four-probe electrical measurement of the NTs were conducted in a Helios 650 dual-beam
23 instrument (Thermo Fisher Scientific) applying a focused-ion beam (FIB)-assisted transfer
24 to the measurement chip and subsequent contacting of the NT with FIB-induced Pt
25 deposition.
26
27

28 Transmission electron microscopy (TEM) and selected area electron diffraction (SAED)
29 patterns analyses were performed using a JEOL JEM2100 microscope operated at 200 kV.
30 The analysis of the TEM images, including intensity profiles along the *c*-axis, and the
31 SAED was performed with Digital Micrograph 3.1.0 (Gatan) software.
32
33

34 X-ray diffraction (XRD) patterns were obtained in a PANalytical Empyrean using the Cu
35 K α line. The samples were freshly prepared by drop casting of powder dispersed in ethanol
36 on a zero-background Si substrate and subsequently analyzed in reflection mode from 4°-
37 90°.
38

39 Two aberration-corrected (probe & image, respectively) Titan microscopes (Thermo Fisher
40 Scientific) were used to perform high-resolution (HR) transmission electron microscopy
41 (TEM) and scanning (S)TEM imaging using high-angle annular dark field (HAADF),
42 annular dark field (ADF) and bright field (BF) detectors. The microscopes were operated
43 at 300 kV and EDS and electron energy-loss spectroscopy (EELS) was applied using the
44 probe-corrected microscope equipped with a high-brightness field emission gun (X-FEG)
45 and respective detectors (EDAX Si(Li) detector, Gatan Tridiem ESR 865 EEL
46 spectrometer). SAED patterns were additionally acquired using the image-corrected Titan
47 microscope.
48
49
50

51 For HRSTEM experiments, the sample powders stored under vacuum were dispersed in
52 ethyl alcohol. For each session, samples were freshly prepared by ultrasonication of the
53 dispersion and drop casting of 2 μ l of the dispersion onto holey carbon TEM copper grids
54 (Quantifoil). To prevent sample contamination under the electron beam, a 14 s plasma
55
56
57

1
2
3 cleaning step was implemented prior to insertion in the microscope. STEM-EDS data was
4 analyzed using the Tia software (Thermo Fisher Scientific) and quantified with the O-K,
5 S-K, Y-K, La-L and Ta-L edges. EELS analysis was performed using a custom Matlab
6 program and the La-M5 (832 eV), Ta-M5 (1735 eV) and Ta-N23 (404 eV), Y-L3 (2080
7 eV) and S-K (2472 eV) edges. Beam damage during EELS acquisition was observed,
8 which increased with the Y content. ImageJ was applied for analysis of the SAED patterns.
9 The aspect ratio of the NTs was determined by TEM analysis of over 20 images of NTs
10 from each sample.
11
12

13 Raman spectroscopy

14
15 A minute quantity of the sample was dispersed in ethanol by sonication and drop casted on
16 the glass substrate used for the Raman analysis. Raman scattering measurements in the
17 range from 100 to 1000 cm^{-1} were recorded on individual NTs using the back-scattering
18 mode. A LabRAM HR Evolution spectrometer (HORIBA, France) equipped with different
19 lasers and the option to manipulate the laser power was used for the analysis. For the
20 633 nm laser the maximum incident power on the sample was 0.225 mW. Given the spot
21 size (1 μm) of the laser, the real incident power on the NT was ~ 0.02 mW. The LabRAM
22 is fitted with an 800 mm spectrograph with a very high spectral resolution and low stray
23 light. Frequency calibration was performed before every measurement session using the Si
24 peak at 520.7 cm^{-1} of single-crystalline Si(100). Initial measurements were recorded with
25 a 600 groves/mm grating with ~ 1.8 cm^{-1} pixel resolution. Subsequently, for a detailed
26 analysis, the measurements were done with 1800 groves/mm grating, with a pixel
27 resolution of ~ 0.35 cm^{-1} . The NTs were illuminated using several microscope objectives
28 (MPlanFL NA=0.9, Olympus, Japan). The system utilizes an open confocal microscope
29 (Olympus BXF) with a spatial resolution better than 1 μm . Due to the very high aspect
30 ratio of the NTs, it is very easy to visualize the single NT with 100x objective. The Raman
31 spectra were collected in a 1024 \times 256 pixel front illuminated CCD camera (Syncerity,
32 HORIBA, USA) with open electrode which was cooled to -60 $^{\circ}\text{C}$. The measurements were
33 done with the laser beam focused on a single NT at a time.
34
35
36
37
38
39

40 FTIR measurements

41
42 Samples for the Fourier transform infrared (FTIR) measurements were prepared by
43 dispensing 2 mg of the MLC (NTs + flakes) in 100 mg KBr powder. The mixed powders
44 were first gently grinded for homogenization and subsequently pressed into circular discs
45 (13 mm) under a pressure of 5 tons. The discs were placed in a vacuum oven and heated to
46 150 $^{\circ}\text{C}$ for 18 h in order to get rid of the adsorbed water (samples which were not properly
47 dried showed clear footprint of water absorption). The samples were measured
48 immediately after drying. Sample Y10 and Y20 were repeated and measured twice. The
49 transmission spectra were recorded using a Thermo Scientific Nicolet 6700 FT-IR
50 spectrometer with 2 cm^{-1} step. The set-up is equipped with DTGS-KBr detector with KBr
51 beamsplitter and KBr disk as a reference. The FTIR chamber was purged by dry nitrogen
52 gas during the measurements. The spectral range of this set-up is 500-7400 cm^{-1} with steps
53
54
55
56
57
58
59
60

of 2 cm⁻¹. The spectra were repeated 200 scans and averaged in order to maximize the signal-to-noise level.

Computational Details

Density-functional theory (DFT) calculations were performed using SIESTA 4.0 software.³⁸ Exchange-correlation potential was described by Generalized Gradient Approximation (GGA) with the Perdew-Burke-Ernzerhof (PBE) parametrization. The core electrons were treated within the frozen core approximation, applying norm-conserving Troullier–Martins pseudopotentials. Only valence shells were accounted for all elements and double- ζ basis set was used for description of the valence orbitals. The k -point mesh was generated by the method of Monkhorst and Pack with a cutoff of 15 Å used for k -point sampling.³⁹ The real-space grid used for the numerical integrations was set to correspond to the energy cutoff of 300 Ry. The calculations were performed using variable-cell and atomic position relaxations, with convergence criteria corresponding to a maximum residual stress of 0.1 GPa for each component of the stress tensor, and maximum residual force component of 0.05 eV/Å.

Preliminary test calculations of binary sulfides LaS, LaS₂, YS, YS₂ and 2H-TaS₂ revealed a good suitability of the chosen approach for describing the geometry. The differences between experimental and computed lattice parameters were found to be within $\pm 2\%$. The enthalpies of formation ΔH at T = 0 K for YS, LaS and LaS₂ from the respective elements were calculated as the difference ΔE between total energies of the compounds and the bulk elements. The theoretically calculated values -4.53 eV/YS, -5.07 eV/LaS and -6.83 eV/LaS₂ are comparable very well with known experimental data for ΔH at T = 298 K: -4.77 eV/YS, -4.73 eV/LaS and -6.46 eV/LaS₂.⁴⁰ Further, the thermodynamic stability of model misfits of the general composition (Y_xLa_{1-x}S)_yTaS₂ has been considered for y = 1.14, 1.20 and 1.25. The supercells of these approximants have been assembled using 16 MS and 14 TaS₂, 12 MS and 10 TaS₂, 20 MS and 16 TaS₂ units (MS = LaS, YS), respectively.

Supporting Information

The supporting information available online provides additional electron microscopy, spectroscopy and diffraction data, statistical information (size, structure parameters) on the NTs as well as Raman spectroscopy, FTIR and DFT results.

Acknowledgments

A.E. acknowledges the support by Act 211 Government of the Russian Federation, contract № 02.A03.21.0006. The support of the Israel Science Foundation (grant No. 7130970101), Irving and Cherna Moskowitz Center for Nano and Bio-Nano Imaging; the Perlman Family Foundation and the Kimmel Center for Nanoscale Science (grant No. 43535000350000) are greatly acknowledged. The HRSTEM and EELS studies as well as some of the ED and TEM investigations were conducted at the Laboratorio de Microscopias Avanzadas, Instituto de Nanociencia de Aragon, Universidad de Zaragoza, Spain. We thank G. Antorrena (LMA-INA) for his help with the XRD acquisition. R.A. gratefully

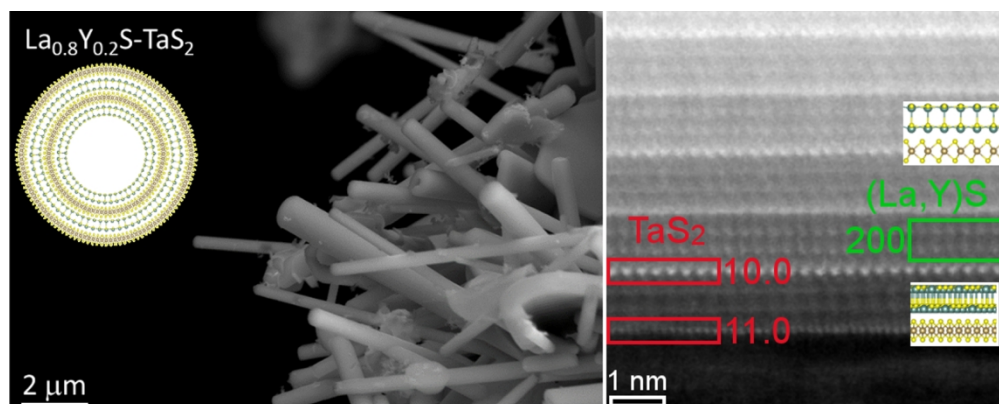
acknowledges the support from the Spanish Ministry of Economy and Competitiveness (MINECO) through project grant MAT2016-79776-P (AEI/FEDER, UE) and from the European Union H2020 program “ESTEEM3” (823717). S.H. acknowledges funding by German Research Foundation (HE 7675/1-1). I.P. is the Sharon Zuckerman Research Fellow Chair.

References

- ¹Tenne, R.; Margulis, L.; Genut, M.; Hodes, G. Polyhedral and Cylindrical Structures of Tungsten Disulphide. *Nature* **1992**, 360, 444–446.
- ²Tenne, R. Inorganic Nanotubes and Fullerene-Like Nanoparticles. *Nat. Nanotechnol.* **2006**, 1, 103–111.
- ³Višić, B.; Panchakarla, L. S.; Tenne, R. Inorganic Nanotubes and Fullerene-like Nanoparticles at the Crossroads between Solid-State Chemistry and Nanotechnology. *J. Am. Chem. Soc.* **2017**, 139, 12865–12878.
- ⁴Serra, M.; Arenal, R.; Tenne, R. An Overview of the Recent Advances in Inorganic Nanotubes. *Nanoscale* **2019**, 11, 8073–8090.
- ⁵Bernaerts, D.; Amelinckx, S.; van Tendeloo, G.; van Landuyt, J. Microstructure and Formation Mechanism of Cylindrical and Conical Scrolls of the Misfit Layer Compounds $PbNbnS_{2n+1}$. *J. Cryst. Growth* **1997**, 172, 433–439.
- ⁶Radovsky, G.; Popovitz-Biro, R.; Staiger, M.; Gartsman, K.; Thomsen, C.; Lorenz, T.; Seifert, G.; Tenne, R. Synthesis of Copious Amounts of SnS_2 and SnS_2/SnS Nanotubes with Ordered Superstructures. *Angew. Chem., Int. Edit.* **2011**, 50, 12316–12320.
- ⁷Radovsky, G.; Popovitz-Biro, R.; Lorenz, T.; Joswig, J.-O.; Seifert, G.; Houben, L.; Dunin-Borkowski, R. E.; Tenne, R. Tubular Structures from the $LnS-TaS_2$ ($Ln = La, Ce, Nd, Ho, Er$) and $LaSe-TaSe_2$ Misfit Layered Compounds. *J. Mater. Chem. C* **2016**, 4, 89–98.
- ⁸Panchakarla, L. S.; Radovsky, G.; Houben, L.; Popovitz-Biro, R.; Dunin-Borkowski, R. E.; Tenne, R. Nanotubes from Misfit Layered Compounds. *J. Phys. Chem. Lett.* **2014**, 5, 3724–3736.
- ⁹Wieggers, G.A. Misfit Layer Compounds. *Prog. Solid State Ch.* **1996**, 24, 1–139.
- ¹⁰Grippa, A.Y.; Lidin, S.; D’yachenko, O. G.; Rupasov, D. P.; Antipov, E. V. Synthesis and Study of Sr-substituted Misfit Layer Sulfides. *Mater. Res. Bull.* **2005**, 40, 79–91.
- ¹¹Meerschaut, A.; Moëlo, Y.; Cario, L.; Lafond, A.; Deudon, C. Charge Transfer in Misfit Layer Chalcogenides, $[(MX)_n]^{1+x}(TX_2)_m$. *Mol. Cryst. Liq. Cryst. A* **2000**, 341, 1–8.
- ¹²Roesky, R.; Meerschaut, A.; van der Lee, A.; Rouxel, J. Structural Study of a Niobium-Lanthanum Sulfide Compound $[(Nb_{1-x}La_xS)NbS_2]$, $x \approx 0.3$; The First “Self-Misfit” Compound]. *Mater. Res. Bull.* **1994**, 29, 1149–1155.
- ¹³Pauling, L. The Structure of the Chlorites. *Proc. Natl. Acad. Sci. U. S. A.* **1930**, 16, 578–582.
- ¹⁴Mitchell, K.; Somers, R. C.; Huang, F. Q.; Ibers, J. A. Syntheses, Structure, and Magnetic Properties of Several $LnYbQ_3$ Chalcogenides, $Q=S, Se$. *J. Solid State Chem.* **2004**, 177, 709–713.

- 1
2
3
4
5
6
7
8
9
10
11
12
13
14
15
16
17
18
19
20
21
22
23
24
25
26
27
28
29
30
31
32
33
34
35
36
37
38
39
40
41
42
43
44
45
46
47
48
49
50
51
52
53
54
55
56
57
58
59
60
- ¹⁵Meerschaut, A.; Rabu, P.; Rouxel, J.; Monceau, P.; Smontara, A. Structural Reinvestigation of (LaS)_{1.14}NbS₂ and Resistivity Measurements. *Mater. Res. Bull.* **1990**, *25*, 855–861.
- ¹⁶Ohno, Y. Lamellar and Filament-Like Crystals of Misfit-Layer Compounds Containing (Sm, Ta, S) and (Pb, Bi, Nb, S) Elements. *J. Solid State Chem.* **2005**, *178*, 1539–1550.
- ¹⁷Hong, S. Y.; Popovitz-Biro, R.; Prior, Y.; Tenne, R. Synthesis of SnS₂/SnS Fullerene-Like Nanoparticles. *J. Am. Chem. Soc.* **2003**, *125*, 10470–10474.
- ¹⁸Lajaunie, L.; Radovsky, G.; Tenne, R.; Arenal, R. Quaternary Chalcogenide-Based Misfit Nanotubes LnS(Se)-TaS(Se)₂ (Ln = La, Ce, Nd, and Ho). *Inorg. Chem.* **2018**, *57*, 747–753.
- ¹⁹Serra, M.; Anumol, E. A.; Stolovas, D.; Pinkas, I.; Joselevich, E.; Tenne, R.; Enyashin, A.; Deepak, F. L. Synthesis and Characterization of Quaternary La(Sr)S-TaS₂ Misfit-Layered Nanotubes. *Beilstein J. Nanotech.* **2019**, *10*, 1112–1124.
- ²⁰Rabu, P.; Meerschaut, A.; Rouxel, J.; Wiegers, G. A. The Crystal Structure of the Misfit Layer Compound (YS)_{1.23}NbS₂. *J. Solid State Chem.* **1990**, *88*, 451–458.
- ²¹Stolovas, D.; Serra, M.; Popovitz-Biro, R.; Pinkas, I.; Houben, L.; Calvino, J. J.; Joselevich, E.; Tenne, R.; Arenal, R.; Lajaunie, L. Nanotubes from the Misfit Compound Alloy LaS-Nb_xTa_(1-x)S₂. *Chem. Mater.* **2018**, *30*, 8829–8842.
- ²²Radovsky, G.; Popovitz-Biro, R.; Tenne, R. Nanotubes from the Misfit Layered Compounds MS-TaS₂, Where M = Pb, Sn, Sb, or Bi. *Chem. Mater.* **2014**, *26*, 3757–3770.
- ²³Meetsma, A.; Wiegers, G. A.; Haange, R. J.; Boer, J. L. de. Structure of 2H-TaS₂. *Acta Crystallogr. C* **1990**, *46*, 1598–1599.
- ²⁴Hulliger, F. and Hull, G. W. Superconductivity in Rocksalt-Type Compounds. *Solid State Commun.* **1970**, *8*, 1379–1382.
- ²⁵Shannon, R. D. Revised Effective Ionic Radii and Systematic Studies of Interatomic Distances in Halides and Chalcogenides. *Acta Cryst. A* **1976**, *32*, 751–767.
- ²⁶Pennycook, S. J. and Nellist, P. D. Scanning Transmission Electron Microscopy. In: *Imaging and Analysis*; Springer: New York, NY, **2011**.
- ²⁷Advanced Transmission Electron Microscopy; Deepak, F. L., Mayoral, A., Arenal, R., Eds.; Springer International Publishing: Cham, Switzerland, **2015**; pp 11-14.
- ²⁸Kisoda, K.; Hangyo, M.; Nakashima, S.; Suzuki, K.; Enoki, T.; Ohno, Y. Raman Scattering from Misfit Layer Compounds (RS)_xTaS₂ (R Identical to La,Ce,Sm or Gd; S Identical to Sulphur; x Approximately=1.2). *J. Phys.: Condens. Matter* **1995**, *7*, 5383–5393.
- ²⁹Staiger, M.; Bačić, V.; Gillen, R.; Radovsky, G.; Gartsman, K.; Tenne, R.; Heine, T.; Maultzsch, J.; Thomsen, C. Raman Spectroscopy of Intercalated and Misfit Layer Nanotubes. *Phys. Rev. B* **2016**, *94*, 35430.
- ³⁰Serra, M.; Stolovas, D.; Houben, L.; Popovitz-Biro, R.; Pinkas, I.; Kampmann, F.; Maultzsch, J.; Joselevich, E.; Tenne, R. Synthesis and Characterization of Nanotubes from Misfit (LnS)_{1+y}TaS₂ (Ln=Pr, Sm, Gd, Yb) Compounds. *Chemistry* **2018**, *24*, 11354–11363.

- 1
2
3
4
5
6
7
8
9
10
11
12
13
14
15
16
17
18
19
20
21
22
23
24
25
26
27
28
29
30
31
32
33
34
35
36
37
38
39
40
41
42
43
44
45
46
47
48
49
50
51
52
53
54
55
56
57
58
59
60
- ³¹Serra, M.; Lajaunie, L.; Sreedhara, M. B.; Miroshnikov, Y.; Pinkas, I.; Calvino, J. J.; Enyashin, A. N.; Tenne, R. Quaternary Ln_xLa_(1-x)S-TaS₂ Nanotubes (Ln=Pr, Sm, Ho, and Yb) as a Vehicle for Improving the Yield of Misfit Nanotubes. *Appl. Mater. Today* **2020**, *19*, 100581.
- ³²Hirata, T. and Ohuchi, F.S. Temperature Dependence of The Raman Spectra of 1T-TaS₂. *Solid State Commun.* **2001**, *117*, 361–364.
- ³³Parkin, S. S. P. and Beal, A. R. 3D Transition Metal Intercalates of the Niobium and Tantalum Dichalcogenides. *Philos. Mag. B* **2006**, *42*, 627–642.
- ³⁴Ruscher, C. H.; Haas, C.; van Smaalen, S.; Wiegers, G. A. Investigation of the Optical Reflectivity of Misfit Layer Compounds. *J. Phys.: Condens. Matter* **1994**, *6*, 2117–2128.
- ³⁵Hangyo, M.; Nishio, T.; Nakashima, S.; Ohno, Y.; Terashima, T.; Kojima, N. Raman and Infrared Spectra of Misfit Layer Compounds MNbS₃ (M=Sn, Pb, La, Ce). *Jpn. J. Appl. Phys.* **1993**, *32*, 581–583.
- ³⁶Hangyo, M.; Kisoda, K.; Nishio, T.; Nakashima, S.; Terashima, T.; Kojima, N. Staging and Interlayer Interaction in the Misfit-Layer Compounds (RS)_nNbS₂ (R=La,Ce; n=0.6,1.2) studied by Raman and Infrared Spectroscopies. *Phys. Rev. B* **1994**, *50*, 12033–12043.
- ³⁷Wooten, F. *Optical Properties of Solids*; Elsevier Science: Burlington, **1972**.
- ³⁸Ordejón; Artacho; Soler. Self-Consistent Order-N Density-Functional Calculations for Very Large Systems. *Phys. Rev. B* **1996**, *53*, R10441-R10444.
- ³⁹Moreno and Soler. Optimal Meshes for Integrals in Real- and Reciprocal-Space Unit Cells. *Phys. Rev. B* **1992**, *45*, 13891–13898.
- ⁴⁰Franke, P. and Neuschütz, D. Binary Systems. Part 3. In: *Binary Systems from Cs-K to Mg-Zr*; Springer-Verlag: Berlin/Heidelberg, **2005**.



20 ToC graphic

21 289x115mm (150 x 150 DPI)